Nonlinear response in a noncentrosymmetric topological insulator

Zhou Li and Franco Nori

Nonlinear response in a non-centrosymmetric topological insulator

Zhou Li[1,2*] and Franco Nori[1,3]

[1] *Theoretical Quantum Physics Laboratory, RIKEN Cluster for Pioneering Research, Wako-shi, Saitama 351-0198, Japan*
[2] *School of Electrical and Computer Engineering and Birck Nanotechnology Center,*
Purdue University, West Lafayette, IN 47907, United States
[3] *Department of Physics, University of Michigan, AnnArbor, Michigan 48109-1040, United States*
(Dated: April 9, 2019)

Nonlinear phenomena are inherent in most systems in nature. Second or higher-order harmonic generations, three-wave and four-wave mixing are typical phenomena in nonlinear optics. To obtain a nonzero signal for second-harmonic generation in the long-wavelength limit ($q \to 0$), the breaking of inversion symmetry is required. In topological materials, a hexagonal warping term which breaks the rotation symmetry of the Fermi surface is observed by angular-resolved photo-emission spectroscopy (ARPES). If a gap opens (e.g., by doping with magnetic impurities) the inversion symmetry will be broken. Here we use a nonlinear response theory based on a generalized Kubo formula to explain the frequency up-conversion in topological materials.

I. INTRODUCTION

The nonlinear response to an external driving electromagnetic field $\mathbf{E}$ or $\mathbf{B}$ can be characterized by a conductivity tensor $\tilde{\sigma}$ which is not a constant, but depends on the magnitude of $\mathbf{E}$ or $\mathbf{B}$. Nonlinearity is often found to be important in optical devices, especially in the recent discovery of high-efficiency solar energy harvesting in non-centrosymmetric crystal structures such as perovskite oxides[1–5]. In 3D topological insulator (TI) and ferroelectric materials, Dirac cones[6–10] obeying spin-momentum locking[11,12] with in-plane spin component perpendicular to the momentum $\mathbf{k}$ were verified by spin-sensitive angular-resolved photo emission spectroscopy (ARPES). The quasiparticles (helical Dirac fermions) observed in topological materials possess an important feature: the Fermi contours are circular for small values of the chemical potential μ, and acquire a snowflake[10] shape as μ increases. Analyzing the experiment results, Fu[13] assigned a hexagonal warping term in the Hamiltonian of such quasiparticles. This term has a strong signature in the optical conductivity, spin texture, Hall conductivity and circular dichroism of topological insulators[14–16].

The optical conductivity was predicted to show[14] a large near-linear increase with photon energy above the inter-band threshold as compared to the usual flat background[17–19] inter-band optical conductivity in graphene. The spin texture[20] (specifically, out of plane spin S_z) shows a mixture of up-and-down directions; in contrast to the normal all-up or all-down hedgehog type[21] distribution for massive Dirac fermions (see, e.g. Fig. 5 of Ref. [16]). It is also possible to introduce a gap in the topological surface quasiparticles (massive Dirac fermions) by magnetic doping[22,23] in Bi_2Se_3[22] and recently in $Cr_x(Bi_{1-y}Sb_y)_{2-x}Te_3$[23,24]. Considerable particle-hole asymmetry of the surface Dirac cone of a 3D TI usually displays, which can be modeled with a small sub-dominant Schrödinger quadratic-in-momentum term in addition to the dominant Dirac Hamiltonian. While perhaps small, the Schrödinger term has been shown to provide important modifications[25] in the chiral nonlinear magneto optical conductivity (MOC) which is related to the absorption of left and right circularly polarised light of 3D TI. This is to be compared with what is found in graphene[26–28] or the related single layer silicene[29].

In this work we focus on the nonlinear optical conductivity induced by an electric field $\mathbf{E}$ in contrast to the nonlinear MOC which is induced by a magnetic field $\mathbf{B}$. We consider three-wave mixing[30] (e.g., second-harmonic generation) from non-centrosymmetric topological materials. Second-harmonic generation (SHG) was first demonstrated by projecting a laser beam through crystalline quartz[31]. Later on this effect was found in other materials (e.g., silicon surfaces)[32] with broken inversion symmetry. Theoretically, SHG was predicted to be nonzero in semiconductors[33], and more recently in single-layer graphene[34,35] with oblique incidence of radiation on the 2D electron layer. For oblique incidence, the incident radiation has a nonzero wave vector component $\mathbf{q}$ parallel to the plane of the 2D layer. In the long-wavelength limit ($\mathbf{q} \to 0$, normal incidence), the SHG vanishes because graphene is a centrosymmetric material. However, higher-order harmonics (e.g., third-harmonic generation) could be nonzero in graphene[36] or generally Dirac Fermions system[37]. The nonlinear coupling of three monochromatic waves, thus called three-wave mixing, has been successfully used to generate optical frequency up-conversion or down-conversion. Nonlinear optical analogs, including SHG, have also been studied recently in various contexts, including Josephson plasma waves[38] and cavity quantum electrodynamics[39–42].

In the following paragraphs we present a Green's function formalism for calculating the nonlinear conductivity in section II. We use a two-band hexagonal warping model which can be found in surface states of 3D TI and ferroelectric materials. The inversion symmetry of the Fermi surface is broken by a magnetic doping in the hexagonal warping model. In section III we present the linear optical conductivity from the Green's function formalism. In section IV we present our numerical results of the nonlinear and linear conductivity for different sets of parameters (e.g., chemical potential, gap parameter,

temperature, etc.). In section V we summarize our results with a conclusion.

II. NONLINEAR OPTICAL CONDUCTIVITY

The linear conductivity $\tilde{\sigma}_{xx}(\omega)$ is related to the current $J_x(\omega) = \tilde{\sigma}_{xx}(\omega)E_x(\omega)$, while the nonlinear conductivity $\tilde{\sigma}_{xxx}(\omega, \omega)$ is related to the current $J_x(2\omega) = \tilde{\sigma}_{xxx}(\omega, \omega)E_x^2(\omega)$. In general, the nonlinear conductivity is a tensor $\tilde{\sigma}_{\alpha\beta\gamma}$. However, here for simplicity we only consider the xxx component of the tensor; the other components of the conductivity tensor can be obtained in a similar way. The nonlinear conductivity has been well studied in earlier references; for example, in Ref. [43] the

Eq. (2-48) defines the nonlinear conductivity as a product of momentum matrix elements and then in Eq. (2-49) the momentum matrix elements were connected to velocity matrix elements.

For the linear conductivity it has been shown in chapter 8 of the book [44] that the Eq. (8.53) uses a trace of momentum operators and Green's functions and then in Eq. (8.55) this was connected to the product of velocity matrix elements. The velocity matrix element is connected to the position matrix element and the shift vector.[45] For the nonlinear conductivity, instead of using velocity matrix elements[43] directly, we define the nonlinear conductivity as a trace of velocity operators and Green's functions[44]; the imaginary frequency in each Green's function is set by using a triangle Feynman diagram.

$$\tilde{\sigma}_{xxx}(\omega, \omega) = \frac{e^3}{\omega^2} \frac{i}{4\pi^2} \int_0^{2\pi} d\theta \int_0^{k_{\text{cut}}} k dk T \sum_l \text{Tr} \langle v_x \widehat{G}(\mathbf{k}, i\omega_l) v_x \widehat{G}(\mathbf{k}, i\omega_l + i\omega_n) v_x \widehat{G}(\mathbf{k}, i\omega_l - i\omega_n) \rangle_{i\omega_n \to \omega + i\delta}, \quad (1)$$

here v_x is the velocity operator and $\widehat{G}(\mathbf{k}, i\omega_l)$ is the matrix Green's function, e is the charge of the electron, k the absolute value of the momentum $\mathbf{k}$ with direction θ and cutoff k_{cut}, T is the temperature with $\omega_n = 2n\pi T$, $\omega_l = (2l+1)\pi T$ the Boson and Fermion Matsubara frequencies, n and l are integers and Tr is a trace. To obtain the nonlinear conductivity, which is a real frequency quantity, we needed to make an analytic continuation from imaginary $i\omega_n$ to real ω and δ is infinitesimal. This is valid for the long wavelength limit $q \to 0$;

Consider a two-band model as an example, the velocity operators and matrix Green's functions are 2×2 matrices, and can be expanded onto the basis of Pauli matrices $\sigma = (\sigma_x, \sigma_y, \sigma_z)$, as $v_x = a_0 + \mathbf{a} \cdot \sigma$, and $\widehat{G}(\mathbf{k}, i\omega_n) = g_0 + \mathbf{g} \cdot \sigma$. We can use the algebra $(\mathbf{a} \cdot \sigma)(\mathbf{g} \cdot \sigma) = (\mathbf{a} \cdot \mathbf{g})I_2 + i(\mathbf{a} \times \mathbf{g}) \cdot \sigma$ to evaluate the trace and the complicated results will be contained in the function $F(k, \theta)$ to be integrated further in momentum space (k, θ). We can also perform the sum over the internal Fermion Matsubara frequencies ω_l and the result is Fermi-Dirac distribution function defined as $f(x) = 1/[\exp(x/T - \mu/T) + 1]$. After tedious but straightforward algebra (details in the appendix), we finally obtained both the inter-band and intra-band nonlinear optical conductivity, the intra-band optical conductivity contributes to the frequency region of $\omega \approx 0$ and was given in the appendix, in the equations below we present the results of the inter-band optical conductivity ($\tilde{\sigma}_{xxx}^{\text{inter}} = \tilde{\sigma}_{xxx}^{\text{inter}}(\omega, \omega)$),

$$\tilde{\sigma}_{xxx}^{\text{inter}} = \frac{ie^3}{\hbar^3 \omega^2 \pi^2} \int k dk d\theta F(k, \theta) \frac{[f(E) - f(-E)]}{E} \left[\frac{1}{\hbar\omega + i\delta + 2E} - \frac{1}{\hbar\omega + i\delta - 2E} + \frac{2}{\hbar\omega + i\delta - E} - \frac{2}{\hbar\omega + i\delta + E} \right] (2)$$

Here E is the quasiparticle energy which depends on the momentum $(k_x, k_y) = (k\cos(\theta), k\sin(\theta))$. Take a two-band hexagonal warping model as an example, the Hamiltonian is given by,

$$H_0 = v_k(k_x\sigma_y - k_y\sigma_x) + \frac{\lambda}{2}(k_+^3 + k_-^3)\sigma_z + M\sigma_z, \quad (3)$$

this model has been used to describe the surface states band structure near the Γ point in the surface Brillouin zone of a 3D TI and also recently in ferroelectric materials. The Dirac fermion velocity to second order is $v_k = \hbar v_F(1 + \alpha k^2)$, with v_F the usual Fermi velocity and $\hbar v_F$ measured to be 2.55 eV·Å and α is a constant which is fit along with m to the measured band structure in Ref. [13]. Here m appears in the quadratic term $\hbar^2 k^2/(2m)$ which, for simplicity, is dropped in the Hamil-

tonian H_0. The inclusion of the quadratic term provides particle-hole asymmetry; however the wave function is not changed[16], thus the Berry curvature and Berry connection (defined from the wave function) are not modified by this quadratic term. For simplicity, the quadratic correction to the velocity α is also discarded. The magnitude of the hexagonal warping parameter is $\lambda =$ 200 eV·Å^3, estimated from the measured Fermi velocity. The same value was used in Ref. [13]. The σ_x, σ_y, σ_z are Pauli matrices here referring to spin, while in graphene these would relate instead to pseudospin. Finally $k_\pm = k_x \pm ik_y$, with the k_x, k_y momentum along the x and y axis, respectively. M is the strength of the gap opened when the topological thin film is in proximity to magnetic impurities.

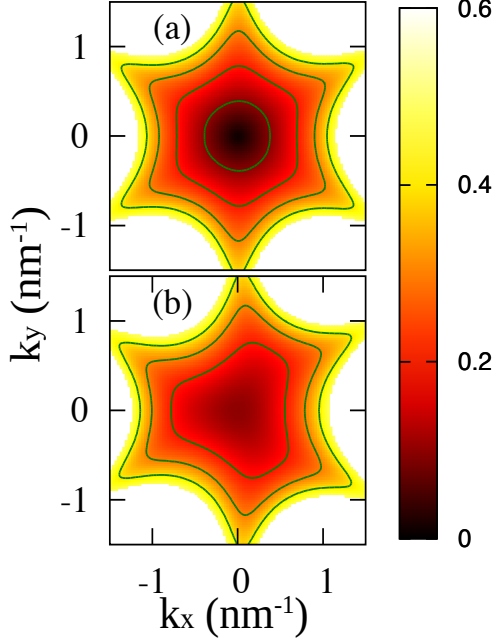The quasiparticle energy dispersion relation is given

FIG. 1. (Color online) Constant-energy contours for the dispersion curves used to describe the surface states in 3D TI. In (a) the gap is $2M=20$ meV, while in (b) the gap is $2M=200$ meV. The chemical potential μ can be changed by doping the 3D TI. The four contours shown in green correspond to different chemical potentials $\mu = 0.1$ eV (in (b) this contour disappears), $\mu = 0.2$ eV, $\mu = 0.3$ eV and $\mu = 0.4$ eV. The k_x and k_y axes are in units of 0.1 Å^{-1}. In (a), for the contour $\mu = 0.1$ eV, one can see the Fermi surface deviate slightly from a perfect circle; and for higher chemical potential, the Fermi surface is a snowflake shape. In (b) the Fermi surface becomes significantly distorted. The hexagonal warping parameter here is $\lambda = 0.2$ eV $\cdot$ (nm)^3.

by $E = \sqrt{v_k^2 k^2 + [\lambda k^3 \cos(3\theta) + M]^2}$, and the function $F(k, \theta)$ is given by

$$F(k,\theta) = \frac{[k_x v_k^2 + 3\lambda(k_x^2 - k_y^2)(M + \lambda k_x(k_x^2 - 3k_y^2))]}{E^3}$$
$$\times v_k^2 [v_k^2 k_y^2 + \lambda^2(4k_x^6 + 9k_x^4 k_y^2 - 18k_x^2 k_y^4 + 9k_y^6)$$
$$-4\lambda M k_x^3 + M^2]. \quad (4)$$

Note that if $M = 0$ or $\lambda = 0$ the integration $\int_0^{2\pi} d\theta \int_0^{k_{\rm cut}} k dk$ will be zero because the integrand is an odd function of k_x. So only when both $M \neq 0$ and $\lambda \neq 0$ we obtain a non-vanishing second-harmonic generation nonlinear conductivity in the long-wavelength limit $q \to 0$.

III. LINEAR OPTICAL CONDUCTIVITY

It is well known[16] that the linear optical conductivity is obtained from the standard Kubo formula in terms of the matrix Green's function and velocity operators, the longitudinal conductivity is given by

$$\tilde{\sigma}_{xx}(\omega) = \frac{e^2}{i\omega} \frac{1}{4\pi^2} \int_0^{k_{cut}} k dk d\theta \times$$
$$T \sum_l \text{Tr}\langle v_x \widehat{G}(\mathbf{k}, i\omega_l) v_x \widehat{G}(\mathbf{k}, i\omega_n + i\omega_l)\rangle_{i\omega_n \to \omega + i\delta} \quad (5)$$

which works out to be

$$\tilde{\sigma}_{xx}^{\rm inter}(\omega) = \frac{ie^2}{4\pi^2 \hbar^2 \omega} \int_0^{k_{cut}} k dk d\theta H(k, \theta)$$
$$\frac{f(E) - f(-E)}{E} \left[\frac{1}{\hbar\omega + i\delta + 2E} - \frac{1}{\hbar\omega + i\delta - 2E} \right] \quad (6)$$

where the function $H(k, \theta)$ is given by

$$H(k,\theta) = \frac{v_k^2}{E}[9\lambda^2 k^6 \cos^2(2\theta) + (M + \lambda k^3 \cos(3\theta))^2 +$$
$$v_k^2 k^2 \sin^2 \theta - 6\lambda k^3 \cos(2\theta) \cos\theta(M + \lambda k^3 \cos(3\theta))] \quad (7)$$

It is interesting to check the units of $H(k, \theta)$ and $F(k, \theta)$. We find that $F(k, \theta) \times k$ and $H(k, \theta)$ have the same unit as $v_k^2 E$. So $\tilde{\sigma}_{xxx}$ has the same unit as $\tilde{\sigma}_{xx} \times e/(\hbar\omega k)$. Then the product of the nonlinear conductivity $\tilde{\sigma}_{xxx}$ and external electric field, $\tilde{\sigma}_{xxx} \times E_x$ has the same unit as $\tilde{\sigma}_{xx}$, as expected.

IV. NUMERICAL RESULTS

To evaluate the nonlinear optical conductivity, we need to perform an integration in momentum space which is restricted by the Fermi-Dirac distribution function $f(x)$. At zero temperature, the restricted area is the Fermi surface shown in Fig. 1. In (a), for a small chemical potential $\mu = 0.1$ eV, the Fermi surface is very close to but not a perfect circle because of the small gap $2M = 20$ meV. At larger chemical potential $\mu = 0.4$ eV, the Fermi surface deviates a bit from a snowflake shape. In (b) a much larger gap $2M = 200$ meV is used and the Fermi surface is significantly distorted. The inversion symmetry is broken in both (a) and (b).

In Fig. 2 and Fig. 3 we plot the numerical results of the real part of the inter-band nonlinear optical conductivity $\tilde{\sigma}_{xxx}^{\rm inter}(\omega, \omega)$ and linear optical conductivity $\tilde{\sigma}_{xx}^{\rm inter}(\omega)$, respectively. In Fig. 2, we find that if the chemical potential μ is smaller than half the gap M, the onset frequency is M. Because the chemical potential μ lies in the gap, the minimum energy for the inter-band transition is $2M$. The energy of absorbing two photons is 2ω, so that the onset frequency $2\omega \geq 2M$. If the chemical potential μ is larger than M, the onset frequency is the chemical potential μ, because in this case $2\omega \geq 2\mu$. There is a small drop in the nonlinear optical conductivity at $\omega = 2\mu$, because this is the onset frequency for another inter-band transition involving one photon absorbing. Thus the number of photons in the process of frequency doubling decreases. For $\omega \geq 2\mu$, curves with different values of μ fall on top of each other.
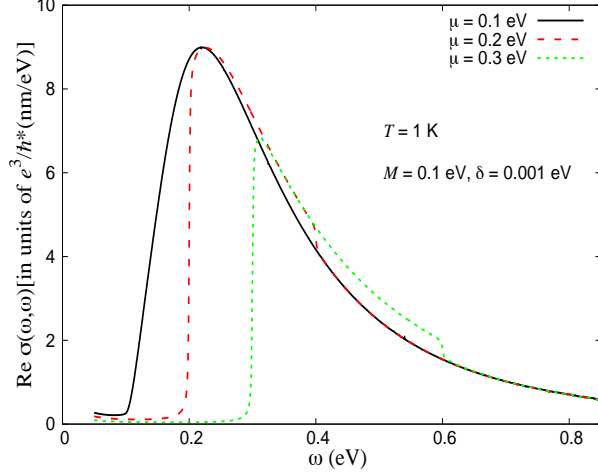
FIG. 2. (Color online) Real part of the nonlinear optical conductivity $\tilde{\sigma}_{xxx}(\omega, \omega)$ versus frequency ω in eV. Three different chemical potentials are used, with black solid for $\mu = 0.1$ eV, red dashed for $\mu = 0.2$ eV and green short dashed for $\mu = 0.3$ eV. The impurity scattering self-energy $\delta = 0.001$ eV and the temperature $T = 1$ K.
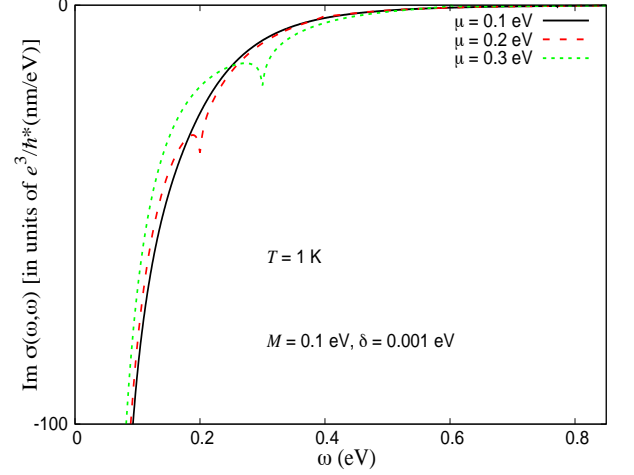

FIG. 4. (Color online) Imaginary part of the nonlinear optical conductivity $\tilde{\sigma}_{xxx}(\omega, \omega)$ versus frequency ω in eV. Three different chemical potentials are considered, with black solid for $\mu = 0.1$ eV, red dashed for $\mu = 0.2$ eV and green short dashed for $\mu = 0.3$ eV. The impurity scattering self energy $\delta = 0.001$ eV and the temperature $T = 1$ K. The sharp drops at $\omega = 0.2$eV and 0.3eV correspond to the sharp jumps in the real part of the conductivity shown in Fig. 2.
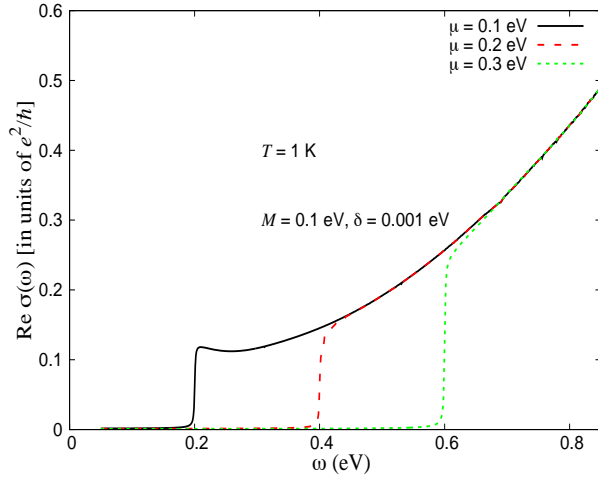

FIG. 3. (Color online) Real part of the linear optical conductivity $\tilde{\sigma}_{xx}(\omega)$ versus frequency ω in eV. Three different chemical potentials are used, with black solid for $\mu = 0.1$ eV, red dashed for $\mu = 0.2$ eV and green short dashed for $\mu = 0.3$ eV. The impurity scattering self-energy $\delta = 0.001$ eV and the temperature $T = 1$ K.
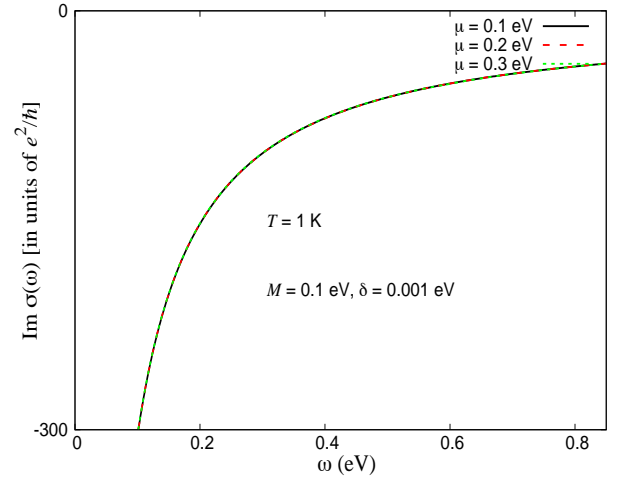

FIG. 5. (Color online) Imaginary part of the linear optical conductivity $\tilde{\sigma}_{xx}(\omega)$ versus frequency ω in eV. Three different chemical potentials are used, with black solid for $\mu = 0.1$ eV, red dashed for $\mu = 0.2$ eV and green short dashed for $\mu = 0.3$ eV. The impurity scattering self energy $\delta = 0.001$ eV and the temperature $T = 1$ K.

In Fig. 3 we find that the onset frequency of the linear optical conductivity is 2μ, in contrast to the onset frequency μ of the nonlinear optical conductivity. When

the frequency ω is larger than the onset frequency 2μ, the linear optical conductivity warps up, in contrast to the nonlinear optical conductivity which decreases as the frequency increases. Curves with different values of μ also fall on top of each other for the linear optical conductivity. In Fig. 4 and Fig. 5 we show the corresponding imaginary parts of the inter-band optical conductivity $\tilde{\sigma}_{xxx}^{\text{inter}}(\omega,\omega)$ and $\tilde{\sigma}_{xx}^{\text{inter}}(\omega)$: respectively. The absolute value of the imaginary part of the nonlinear conductivity decreases to zero faster than that of the linear conductivity.

V. CONCLUSION

In conclusion, we developed a method based on the trace of the velocity operator and Green's function to calculate the nonlinear response functions in a noncentrosymmetric topological insulator. Our method is equivalent to the velocity matrix element method[43] if a two-band free-electron approximation was considered. We obtained the nonlinear conductivity for frequency up-conversion in the second harmonic generation. In the model used here (the two-band hexagonal warping model), the energy scale is around 200 meV in the far-infrared region, relevant for the thermal energy. This model describes surface states of 3D TI. If the 3D TI $(\text{Bi}_{1-y}\text{Sb}_y)_2\text{Te}_3$ (BST) is doped with magnetic impurities, a small gap is opened in $\text{Cr}_x(\text{Bi}_{1-y}\text{Sb}_y)_{2-x}\text{Te}_3$ (CBST)[23,24] thus the inversion symmetry was broken.

* zli5@ualberta.ca

[1] I. Grinberg, D. V. West, M. Torres, G. Gou, D. M. Stein, L. Wu, G. Chen, E. M. Gallo, A. R. Akbashev, P. K. Davies, J. E. Spanier, A. M. Rappe, Perovskite oxides for visible light-absorbing ferroelectric and photovoltaic materials, Nature **503**, 509–512 (2013).

[2] W. Nie, H. Tsai, R. Asadpour, J.-C. Blancon, A. J. Neukirch, G. Gupta, J. J. Crochet, M. Chhowalla, S. Tretiak, M. A. Alam, H.-L. Wang, A. D. Mohite, High-efficiency solution processed perovskite solar cells with millimeter-scale grains, Science **347**, 522–525 (2015).

[3] D. Shi, V. Adinolfi, R. Comin, M. Yuan, E. Alarousu, A. Buin, Y. Chen, S. Hoogland, A. Rothenberger, K. Katsiev, Y. Losovyj, X. Zhang, P. A. Dowben, O. F. Mohammed, E. H. Sargent, O. M. Bakr, Low trap-state density and long carrier diffusion in organolead trihalide perovskite single crystals, Science **347**, 519–522 (2015).

[4] D. W. de Quilettes, S. M. Vorpahl, S. D. Stranks, H. Nagaoka, G. E. Eperon, M. E. Ziffer, H. J. Snaith, D. S. Ginger, Impact of microstructure on local carrier lifetime in perovskite solar cells, Science **348**, 683–686 (2015).

[5] A. M. Cook, B. M. Fregoso, F. de Juan, S. Coh and J. E. Moore, Design principles for shift current photovoltaics, Nature Communications **8**, 14176 (2017).

[6] M. Z. Hasan and C. L. Kane, Colloquium: Topological insulators, Rev. Mod. Phys. **82**, 3045 (2010).

[7] X.-L. Qi and S.-C. Zhang, Topological insulators and superconductors, Rev. Mod. Phys. **83**, 1057 (2011).

[8] J. E. Moore, The birth of topological insulators, Nature **464**, 194 (2010).

[9] D. Hsieh, Y. Xia, L. Wray, D. Qian, A. Pal, J. H. Dil, J. Osterwalder, F. Meier, G. Bihlmayer, C. L. Kane, Y. S. Hor, R. J. Cava, M. Z. Hasan, Observation of Unconventional Quantum Spin Textures in Topological Insulators, Science **323**, 919 (2009).

[10] Y. L. Chen, J. G. Analytis, J.-H. Chu, Z. K. Liu, S.-K. Mo, X. L. Qi, H. J. Zhang, D. H. Lu, X. Dai, Z. Fang, S. C. Zhang, I. R. Fisher, Z. Hussain and Z.-X. Shen, Experimental Realization of a Three-Dimensional Topological Insulator, Bi_2Te_3, Science **325**, 178 (2009).

[11] D. Hsieh, Y. Xia, D. Qian, L. Wray, J. H. Dil, F. Meier, J. Osterwalder, L. Patthey, J. G. Checkelsky, N. P. Ong, A. V. Fedorov, H. Lin, A. Bansil, D. Grauer, Y. S. Hor, R. J. Cava and M. Z. Hasan, A tunable topological insulator in the spin helical Dirac transport regime, Nature(London) **460**, 1101 (2009).

[12] Konstantin Y. Bliokh, Daria Smirnova and Franco Nori, Quantum spin Hall effect of light, Science **348**, 1448 (2015).

[13] L. Fu, Hexagonal Warping Effects in the Surface States of the Topological Insulator Bi_2Te_3, Phys. Rev. Lett **103**, 266801 (2009).

[14] Zhou Li and J. P. Carbotte, Hexagonal warping on optical conductivity of surface states in topological insulator Bi_2Te_3, Phys. Rev. B **87**, 155416 (2013).

[15] X. Xiao and W. Wen, Optical conductivities and signatures of topological insulators with hexagonal warping, Phys. Rev. B. **88**, 045442 (2013).

[16] Zhou Li and J. P. Carbotte, Hexagonal warping on spin texture, Hall conductivity, and circular dichroism of topological insulators, Phys. Rev. B **89**, 165420 (2014).

[17] V. P. Gusynin, S. G. Sharapov and J. P. Carbotte, Anomalous Absorption Line in the Magneto-Optical Response of Graphene, Phys. Rev. Lett. **98**, 157402 (2007).

[18] Z. Q. Li, E. A. Henriksen, Z. Jiang, Z. Hao, M. C. Martin, P. Kim, H. L. Stormer and D. N. Basov, Dirac charge dynamics in graphene by infrared spectroscopy, Nature Phys. **4**, 532 (2008).

[19] M. Orlita and M. Potemski, Dirac electronic states in graphene systems: Optical spectroscopy studies, Semicond. Sci. Technol. **25**, 063001 (2010).

[20] S. Y. Xu, Y. Xia, L. A. Wray, S. Jia, F. Meier, J. H. Dil, J. Osterwalder, B. Slomski, A. Bansil, H. Lin, R. J. Cava and M. Z. Hasan, Topological Phase Transition and Texture Inversion in a Tunable Topological Insulator, Science **332**, 560 (2011).

[21] S. Y. Xu, M. Neupane, C. Liu, D. Zhang, A. Richardella, L. Andrew Wray, N. Alidoust, M. Leandersson, T. Balasubramanian, J. Sánchez-Barriga, O. Rader, G. Landolt, B. Slomski, J. H. Dil, J. Osterwalder, T.-R. Chang, H.-T. Jeng, H. Lin, A. Bansil, N. Samarth and M. Zahid Hasan, Hedgehog spin texture and Berry's phase tuning in a magnetic topological insulator, Nature Phys. **8**,616 (2012).

[22] Y. L. Chen, J.-H. Chu, J. G. Analytis, Z. K. Liu, K. Igarashi, H.-H. Kuo, X. L. Qi, S. K. Mo, R. G. Moore, D. H. Lu, M. Hashimoto, T. Sasagawa, S. C. Zhang, I. R. Fisher, Z. Hussain, Z. X. Shen, Massive Dirac Fermion on the Surface of a Magnetically Doped Topological Insulator, Science **329**, 659 (2010).

[23] K. N Okada, Y. Takahashi, M. Mogi, R. Yoshimi, A. Tsukazaki, K. S. Takahashi, N. Ogawa, M. Kawasaki and Y. Tokura, Observation of topological Faraday and Kerr rotations in quantum anomalous Hall state by terahertz magneto-optics. Nature Communications 7:12245 (2016).

[24] K. Yasuda, A. Tsukazaki, R. Yoshimi, K. S. Takahashi, M. Kawasaki, and Y. Tokura, Large Unidirectional Magnetoresistance in a Magnetic Topological Insulator. Phys. Rev. Lett. **117**, 127202 (2016).

[25] Zhou Li and J. P. Carbotte, Magneto-optical conductivity in a topological insulator, Phys. Rev. B **88**, 045414 (2013).

[26] V. P. Gusynin, S. G. Sharapov and J. P. Carbotte, Magneto-optical conductivity in Graphene, J. Phys. Condens. Matter **19**, 026222 (2007).

[27] Di Xiao, W. Yao and Q. Niu, Valley-Contrasting Physics in Graphene: Magnetic Moment and Topological Transport, Phys. Rev. Lett. **99**, 236809 (2007).

[28] W. Yao, D. Xiao and Q. Niu, Valley-dependent optoelectronics from inversion symmetry breaking, Phys. Rev. B. **77**, 235406 (2008).

[29] C. J. Tabert and E. J. Nicol, Valley-Spin Polarization in the Magneto-Optical Response of Silicene and Other Similar 2D Crystals, Phys. Rev. Lett. **110**, 197402 (2013).

[30] Y. R. Shen, The Principles of Nonlinear Optics (Wiley, 1984).

[31] P. A. Franken, A. E. Hill, C. W. Peters, and G. Weinreich, Generation of Optical Harmonics, Phys. Rev. Lett. **7**, 118 (1961).

[32] H. W. K. Tom, T. F. Heinz, and Y. R. Shen, Second-Harmonic Reflection from Silicon Surfaces and Its Relation to Structural Symmetry, Phys. Rev. Lett. **51**, 1983 (1983).

[33] J. E. Sipe and E. Ghahramani, Nonlinear optical response of semiconductors in the independent-particle approximation, Phys. Rev. B **48**, 11705 (1993).

[34] S. A. Mikhailov, Theory of the giant plasmon-enhanced second-harmonic generation in graphene and semiconductor two-dimensional electron systems, Phys. Rev. B. **8**4, 045432 (2011).

[35] Daria Smirnova and Yuri S. Kivshar, Second-harmonic generation in subwavelength graphene waveguides, Phys. Rev. B. **90**, 165433 (2014).

[36] A. R. Wright, X. G. Xu, J. C. Cao, C. Zhang, Strong nonlinear optical response of graphene in the terahertz regime, App. Phys. Lett. **95**, 072101 (2009).

[37] T. Morimoto and N. Nagaosa, Scaling laws for nonlinear electromagnetic responses of Dirac fermion, Phys. Rev. B **93**, 125125 (2016).

[38] S. Savel'ev, A. L. Rakhmanov, V. A. Yampol'skii, F. Nori, Analogues of nonlinear optics using terahertz Josephson plasma waves in layered superconductors, Nature Physics **2**, 521-525 (2006)

[39] A. F. Kockum, A. Miranowicz, V. Macrí, S. Savasta, F. Nori, Deterministic quantum nonlinear optics with single atoms and virtual photons, Phys. Rev. A **95**, 063849 (2017).

[40] A. F. Kockum, V. Macrí, L. Garziano, S. Savasta, F. Nori, Frequency conversion in ultrastrong cavity QED, Scientific Reports **7**, 5313 (2017).

[41] R. Stassi, V. Macrí, A. F. Kockum, O.D. Stefano, A. Miranowicz, S. Savasta, F. Nori, Quantum Nonlinear Optics without Photons, Phys. Rev. A **96**, 023818 (2017).

[42] X. Gu, A. F. Kockum, A. Miranowicz, Y.X. Liu, F. Nori, Microwave photonics with superconducting quantum circuits Physics Reports 718-719, pp. 1-102 (2017).

[43] N. Bloembergen, Nonlinear optics (W. A. Benjamin Inc., New York, 1965).

[44] E.N. Economou, Green's functions in quantum physics, Third edition, Springer Series in Solid-State Science, (2006).

[45] Zhou Li and F. Nori, in preparation.

Appendix A: Derivation of the nonlinear optical conductivity from the Green's function technique

In this appendix we present a general formula for the calculation of the nonlinear conductivity tensor. We also expand the imaginary frequency Green's function into a sum of the real frequency spectral function which can be measured directly from ARPES experiments. From this expansion we derive the intra-band and inter-band contribution to the nonlinear conductivity. We present how to perform the sum in imaginary frequency and obtain concise results in the non-interacting electron approximation. Consider the hexagonal warping model as an example. The Green's function can be rewritten in the basis of Pauli matrices

$$\widehat{G}(\mathbf{k}, i\omega_n) = \frac{1}{2} \sum_{s=\pm} (1 + s\mathbf{F}_k \cdot \sigma)G_0(\mathbf{k}, s, i\omega_n), \quad \text{(A1)}$$

where

$$\mathbf{F}_k = \frac{(-v_k k \sin\theta, v_k k \cos\theta, \lambda k^3 \cos(3\theta) + M)}{\sqrt{v_k^2 k^2 + [\lambda k^3 \cos(3\theta) + M]^2}},$$

and $G_0(\mathbf{k}, s, i\omega_n) = [i\omega_n + \mu - sE]^{-1}$, where $s = \pm 1$ and the energy spectrum is given by

$$E = \sqrt{v_k^2 k^2 + [\lambda k^3 \cos(3\theta) + M]^2}.$$

The velocity operator can be obtained as (for simplicity we set $\hbar = 1$)

$$
\begin{aligned}
v_x &= \frac{\partial H_0}{\partial k_x} = v_k \sigma_y + \frac{\lambda}{2}(3k_+^2 + 3k_-^2)\sigma_z \\
&= v_k \sigma_y + 3\lambda k^2 \cos(2\theta)\sigma_z \\
v_y &= \frac{\partial H_0}{\partial k_y} = -v_k \sigma_x + \frac{\lambda}{2}(3ik_+^2 - 3ik_-^2)\sigma_z \\
&= -v_k \sigma_x - 3\lambda k^2 \sin(2\theta)\sigma_z \,. \quad \text{(A2)}
\end{aligned}
$$

In general $v_x = a_0 + \mathbf{a} \cdot \sigma$, $v_y = b_0 + \mathbf{b} \cdot \sigma$, and

$\widehat{G}(\mathbf{k}, i\omega_n) = g_0 + \mathbf{g} \cdot \sigma$. If we define $\mathbf{A} = (a_0, \mathbf{a})$, $\mathbf{B} = (b_0, \mathbf{b})$, $\mathbf{G} = (g_0, \mathbf{g})$, and use the following rules for dot and cross product of two vectors

$$
\mathbf{A} \cdot \mathbf{B} = a_0 b_0 + \mathbf{a} \cdot \mathbf{b} \,,
$$

$$
\mathbf{A} \times \mathbf{B} = a_0 \mathbf{b} + b_0 \mathbf{a} + i(\mathbf{a} \times \mathbf{b}) \,.
$$

Then the products of $v_x \widehat{G}(\mathbf{k},\omega_1)$ can be evaluated as

$$
\begin{aligned}
(a_0 + \mathbf{a} \cdot \sigma)(g_{01} + \mathbf{g_1} \cdot \sigma) &= a_0 g_{01} + g_{01}\mathbf{a} \cdot \sigma + a_0 \mathbf{g_1} \cdot \sigma + \mathbf{a} \cdot \mathbf{g_1} + i(\mathbf{a} \times \mathbf{g_1}) \cdot \sigma \\
&= \mathbf{A} \cdot \mathbf{G_1} + (\mathbf{A} \times \mathbf{G_1}) \cdot \sigma \,.
\end{aligned}
$$

The trace can be carried out in general as

$$
\begin{aligned}
&\mathrm{Tr}\langle (a_0 + \mathbf{a} \cdot \sigma)(g_{01} + \mathbf{g_1} \cdot \sigma)(a_0 + \mathbf{a} \cdot \mathbf{p})(g_{02} + \mathbf{g_2} \cdot \sigma)(a_0 + \mathbf{a} \cdot \sigma)(g_{03} + \mathbf{g_3} \cdot \sigma)\rangle \\
=&\mathrm{Tr}\langle (\mathbf{A} \cdot \mathbf{G_1} + (\mathbf{A} \times \mathbf{G_1}) \cdot \sigma)(\mathbf{A} \cdot \mathbf{G_2} + (\mathbf{A} \times \mathbf{G_2}) \cdot \sigma)(\mathbf{A} \cdot \mathbf{G_3} + (\mathbf{A} \times \mathbf{G_3}) \cdot \sigma)\rangle \\
=&[(\mathbf{A} \cdot \mathbf{G_1})(\mathbf{A} \cdot \mathbf{G_2}) + (A \times G_1) \cdot (A \times G_2)](\mathbf{A} \cdot \mathbf{G_3}) + [(\mathbf{A} \cdot \mathbf{G_2})(\mathbf{A} \times \mathbf{G_1}) + (\mathbf{A} \cdot \mathbf{G_1})(\mathbf{A} \times \mathbf{G_2})] \cdot (A \times G_3) \\
&+ i(A \times G_1) \times (A \times G_2) \cdot (A \times G_3) \,.
\end{aligned}
$$

The matrix Green's function $\widehat{G}(\mathbf{k}, i\omega_n)$ can be conveniently written in terms of a matrix spectral function $\widehat{A}(\mathbf{k}, \omega)$ with

$$
\widehat{G}(\mathbf{k}, i\omega_n) = \int_{-\infty}^{\infty} \frac{d\omega}{2\pi} \frac{\widehat{A}(\mathbf{k}, \omega)}{i\omega_n - \omega} \,, \quad \text{(A3)}
$$

then the conductivity in the long-wavelength limit becomes

$$
\begin{aligned}
\tilde{\sigma}_{xxx}(\omega, \omega) = &\frac{e^3}{\omega^2} \frac{i}{4\pi^2} \int_0^{k_{\text{cut}}} k\,dk\,d\theta \int_{-\infty}^{\infty} \frac{d\omega_1}{2\pi} \int_{-\infty}^{\infty} \frac{d\omega_2}{2\pi} \int_{-\infty}^{\infty} \frac{d\omega_3}{2\pi} \\
&\times T \sum_l \frac{1}{i\omega_l - \omega_1} \frac{1}{i\omega_l + i\omega_n - \omega_2} \frac{1}{i\omega_l - i\omega_n - \omega_3} \\
&\times \mathrm{Tr}\langle v_x \widehat{A}(\mathbf{k},\omega_1) v_x \widehat{A}(\mathbf{k},\omega_2) v_x \widehat{A}(\mathbf{k},\omega_3)\rangle_{i\omega_n \to \omega + i\delta} \,,
\end{aligned} \quad \text{(A4)}
$$

For two-band models, the spectral function $\widehat{A}(\mathbf{k}, \omega)$ can be expanded in the basis of Pauli matrices,

$$
\widehat{A}(\mathbf{k}, \omega) = A_I(\mathbf{k},\omega) + A_x(\mathbf{k},\omega)\sigma_x + A_y(\mathbf{k},\omega)\sigma_y + A_z(\mathbf{k},\omega)\sigma_z \,.
$$

In the free-electron approximation (ignoring impurity scattering and electron-phonon scattering), the spectral functions are given by

$$
A_I(\mathbf{k},\omega) = \delta(\omega + \mu - E) + \delta(\omega + \mu + E) \,, \quad \text{(A5)}
$$

$$
A_x(\mathbf{k},\omega) = \frac{-v_k k \sin\theta[\delta(\omega + \mu - E) - \delta(\omega + \mu + E)]}{\sqrt{v_k^2 k^2 + [\lambda k^3 \cos(3\theta) + M]^2}} \,, \quad \text{(A6)}
$$

$$
A_y(\mathbf{k},\omega) = \frac{v_k k \cos\theta[\delta(\omega + \mu - E) - \delta(\omega + \mu + E)]}{\sqrt{v_k^2 k^2 + [\lambda k^3 \cos(3\theta) + M]^2}} \,, \quad \text{(A7)}
$$

$$
A_z(\mathbf{k},\omega) = \frac{[\lambda k^3 \cos(3\theta) + M][\delta(\omega + \mu - E) - \delta(\omega + \mu + E)]}{\sqrt{v_k^2 k^2 + [\lambda k^3 \cos(3\theta) + M]^2}} \,. \quad \text{(A8)}
$$

The trace can be carried out as

$$
\begin{aligned}
&\mathrm{Tr}\langle v_x \widehat{A}(\mathbf{k},\omega_1) v_x \widehat{A}(\mathbf{k},\omega_2) v_x \widehat{A}(\mathbf{k},\omega_3)\rangle \\
&= 8F(k,\theta)[\delta(\omega_1+\mu-E)\delta(\omega_2+\mu+E)\delta(\omega_3+\mu-E) + \delta(\omega_1+\mu+E)\delta(\omega_2+\mu-E)\delta(\omega_3+\mu-E) \\
&\quad + \delta(\omega_1+\mu-E)\delta(\omega_2+\mu-E)\delta(\omega_3+\mu+E) - \delta(\omega_1+\mu-E)\delta(\omega_2+\mu+E)\delta(\omega_3+\mu+E) \\
&\quad - \delta(\omega_1+\mu+E)\delta(\omega_2+\mu-E)\delta(\omega_3+\mu+E) - \delta(\omega_1+\mu+E)\delta(\omega_2+\mu+E)\delta(\omega_3+\mu-E)] \\
&\quad + 8F_{\mathrm{intra}}(k,\theta)[\delta(\omega_1+\mu-E)\delta(\omega_2+\mu-E)\delta(\omega_3+\mu-E) - \delta(\omega_1+\mu+E)\delta(\omega_2+\mu+E)\delta(\omega_3+\mu+E)],
\end{aligned} \tag{A9}
$$

where we have defined two functions,

$$
\begin{aligned}
F(k,\theta) &= \frac{[k_x v_k^2 + 3\lambda(k_x^2 - k_y^2)(M + \lambda k_x(k_x^2 - 3k_y^2))]}{[v_k^2 k^2 + (\lambda k^3 \cos(3\theta) + M)^2]^{3/2}} \\
&\quad \times v_k^2[v_k^2 k_y^2 + \lambda^2(4k_x^6 + 9k_x^4 k_y^2 - 18k_x^2 k_y^4 + 9k_y^6) \\
&\quad\quad - 4\lambda M k_x^3 + M^2],
\end{aligned} \tag{A10}
$$

$$
\begin{aligned}
F_{\mathrm{intra}}(k,\theta) &= \frac{[k_x v_k^2 + 3\lambda(k_x^2 - k_y^2)(M + \lambda k_x(k_x^2 - 3k_y^2))]}{[v_k^2 k^2 + (\lambda k^3 \cos(3\theta) + M)^2]^{3/2}} \\
&\quad \times [k_x(v_k^2 + 3\lambda^2(k_x^4 - 4k_x^2 k_y^2 + 3k_y^4)) + 3\lambda M(k_x^2 - k_y^2)]^2.
\end{aligned} \tag{A11}
$$

These terms can be separated into inter-band and intra-band contributions to the nonlinear conductivity.

Appendix B: Intra-band nonlinear conductivity

The intra-band nonlinear conductivity includes those terms proportional to $\delta(\omega_1+\mu-E)\delta(\omega_2+\mu-E)\delta(\omega_3+\mu-E)$ and $\delta(\omega_1+\mu+E)\delta(\omega_2+\mu+E)\delta(\omega_3+\mu+E)$, which will contribute to the zero-frequency DC conductivity. Performing the sum over Matsubara frequencies, we obtain

$$
\begin{aligned}
&T\sum_l \frac{1}{i\omega_l - \omega_1}\frac{1}{i\omega_l + i\omega_{n1} - \omega_2}\frac{1}{i\omega_l - i\omega_{n2} - \omega_3} \\
&= T\sum_l \frac{1}{i\omega_{n1} - \omega_2 + \omega_1}\left(\frac{1}{i\omega_l - \omega_1} - \frac{1}{i\omega_l + i\omega_{n1} - \omega_2}\right)\frac{1}{i\omega_l - i\omega_{n2} - \omega_3} \\
&= T\sum_l \frac{1}{i\omega_{n1} - \omega_2 + \omega_1}\left[\frac{1}{-i\omega_{n2} - \omega_3 + \omega_1}\left(\frac{1}{i\omega_l - \omega_1} - \frac{1}{i\omega_l - i\omega_{n2} - \omega_3}\right)\right. \\
&\quad \left. - \frac{1}{-i\omega_{n1} - i\omega_{n2} - \omega_3 + \omega_2}\left(\frac{1}{i\omega_l + i\omega_{n1} - \omega_2} - \frac{1}{i\omega_l - i\omega_{n2} - \omega_3}\right)\right] \\
&= \frac{1}{i\omega_{n1} - \omega_2 + \omega_1}\left[\frac{f(\omega_3) - f(\omega_1)}{i\omega_{n2} + \omega_3 - \omega_1} + \frac{f(\omega_2) - f(\omega_3)}{i\omega_{n1} + i\omega_{n2} + \omega_3 - \omega_2}\right].
\end{aligned}
$$

And the intra-band conductivity becomes

$$
\begin{aligned}
\tilde{\sigma}_{xxx}(\omega,\omega)_{\mathrm{intra}} &= \frac{e^3}{\omega^2}\frac{8i}{4\pi^2}\int_0^{k_{\mathrm{cut}}} k\,dk\,d\theta \int_{-\infty}^{\infty}\frac{d\omega_1}{2\pi}\int_{-\infty}^{\infty}\frac{d\omega_2}{2\pi}\int_{-\infty}^{\infty}\frac{d\omega_3}{2\pi} F_{\mathrm{intra}}(k,\theta) \\
&\quad \times [\delta(\omega_1+\mu-E)\delta(\omega_2+\mu-E)\delta(\omega_3+\mu-E) - \delta(\omega_1+\mu+E)\delta(\omega_2+\mu+E)\delta(\omega_3+\mu+E)] \\
&\quad \times \frac{1}{\omega+i\delta - \omega_2 + \omega_1}\left[\frac{f(\omega_3) - f(\omega_1)}{\omega+i\delta + \omega_3 - \omega_1} + \frac{f(\omega_2) - f(\omega_3)}{2\omega + 2i\delta + \omega_3 - \omega_2}\right],
\end{aligned} \tag{B1}
$$

the intra-band conductivity can be numerically evaluated, by replacing the δ function with the broadened Lorentzian function. One can also evaluate the intra-band conductivity analytically; one example was given in the appendix of Ref. [14].

Appendix C: Inter-band nonlinear conductivity

The other terms like $\delta(\omega_1+\mu-E)\delta(\omega_2+\mu+E)\delta(\omega_3+\mu-E)$ are included in the inter-band nonlinear conductivity which will contribute to the nonzero-frequency AC conductivity, written as

$$\tilde{\sigma}_{xxx}(\omega,\omega)_{\text{inter}} = \frac{e^3}{\omega^2}\frac{8i}{4\pi^2}\int_0^{k_{\text{cut}}} kdkd\theta F(k,\theta)\Big[\frac{1}{\omega+i\delta+2E}\Big(\frac{f(-E)-f(E)}{2\omega+2i\delta+2E}\Big) + \frac{1}{\omega+i\delta-2E}\Big(\frac{f(E)-f(-E)}{\omega+i\delta+2E}\Big)$$

$$+\frac{1}{\omega+i\delta}\Big(\frac{f(-E)-f(E)}{\omega+i\delta-2E} + \frac{f(E)-f(-E)}{2\omega+2i\delta-2E}\Big) - \frac{1}{\omega+i\delta+2E}\Big(\frac{f(-E)-f(E)}{\omega+i\delta-2E}\Big)$$

$$-\frac{1}{\omega+i\delta-2E}\Big(\frac{f(E)-f(-E)}{2\omega+2i\delta-2E}\Big) - \frac{1}{\omega+i\delta}\Big(\frac{f(E)-f(-E)}{\omega+i\delta+2E} + \frac{f(-E)-f(E)}{2\omega+2i\delta+2E}\Big)\Big],$$

which is further simplified as

$$\tilde{\sigma}_{xxx}(\omega,\omega)_{\text{inter}} = \frac{2ie^3}{\omega^2\pi^2}\int_0^{k_{\text{cut}}} kdkd\theta F(k,\theta)$$

$$\times\Big[\frac{2}{\omega+i\delta-2E}\frac{f(E)-f(-E)}{\omega+i\delta+2E} - \frac{f(E)-f(-E)}{\omega+i\delta-2E}\frac{1}{\omega+i\delta-E} - \frac{f(E)-f(-E)}{\omega+i\delta+2E}\frac{1}{\omega+i\delta+E}\Big].$$

Finally we obtained

$$\tilde{\sigma}_{xxx}(\omega,\omega)_{\text{inter}} \quad = \quad \frac{ie^3}{\omega^2\pi^2}\int_0^{2\pi} d\theta \int_0^{k_{\text{cut}}} kdk\frac{[f(E)-f(-E)]}{E}$$

$$\times F(k,\theta)\Big[\frac{1}{\omega+i\delta+2E} - \frac{1}{\omega+i\delta-2E} + \frac{2}{\omega+i\delta-E} - \frac{2}{\omega+i\delta+E}\Big]. \tag{C1}$$